QUANTUM GASES

Observation of the Efimovian expansion in scale-invariant Fermi gases

Shujin Deng,[1]* Zhe-Yu Shi,[2]* Pengpeng Diao,[1] Qianli Yu,[1] Hui Zhai,[2] Ran Qi,[3]† Haibin Wu[1,4]†

Scale invariance plays an important role in unitary Fermi gases. Discrete scaling symmetry manifests itself in quantum few-body systems such as the Efimov effect. Here, we report on the theoretical prediction and experimental observation of a distinct type of expansion dynamics for scale-invariant quantum gases. When the frequency of the harmonic trap holding the gas decreases continuously as the inverse of time *t*, the expansion of the cloud size exhibits a sequence of plateaus. The locations of these plateaus obey a discrete geometric scaling law with a controllable scale factor, and the expansion dynamics is governed by a log-periodic function. This marked expansion shares the same scaling law and mathematical description as the Efimov effect.

Interaction between dilute ultracold atoms is described by the s-wave scattering length. For a spin-1/2 Fermi gas, when the scattering length diverges at a Feshbach resonance, there is no length scale other than the interparticle spacing in this many-body system, and therefore the system, known as the unitary Fermi gas, becomes scale invariant. The spatial scale invariance leads to universal thermodynamics and transport properties, as revealed by many experiments (*1*–*13*). On the other hand, in a boson system with an infinite scattering length, three-body bound states can form, where the extra length scale of the three-body parameter turns the continuous scaling symmetry into a discrete scaling symmetry and gives rise to an infinite number of three-body bound states whose energies obey a geometric scaling symmetry. This so-called Efimov effect (*14*, *15*) has been observed in cold atom experiments (*16*–*23*), with recent work confirming the geometric scaling of the energy spectrum (*24*–*27*).

For a harmonic trapped gas, the expansion dynamics offers great insight to the property of the gas (*28*–*33*). Here, we consider what happens to a scale-invariant quantum gas held in a harmonic trap when the trap is gradually opened up by decreasing the trap frequency ω as $1/(\sqrt{\lambda}t)$, where λ is a constant and t is time (Fig. 1, A and B). Naïvely, by dimensional analysis, one would expect that the cloud size $\mathcal{R}$ just increases as $\sqrt{t}$. Here we show, both theoretically and experimentally, that when λ is smaller than a critical value, the expansion dynamics displays a discrete scaling symmetry in the time domain. As a function of t, $\mathcal{R}$ displays a sequence of plateaus, which means that at a set of discrete times t_n the cloud expansion stops, despite the continuous decreasing of the trap frequency. The locations of the plateaus t_n obey a geometric scaling behavior.

To explain these dynamics, we first point out why $\omega = 1/(\sqrt{\lambda}t)$ is special. For simplicity, we first consider a three-dimensional (3D) isotropic trap $V(r) = m\omega^2 r^2/2$. In the absence of a trapping potential, the system is invariant under a scale transformation $r \to \Lambda r$, whereas in the presence of a static harmonic trap, the fixed harmonic length introduces an additional length scale that breaks this spatial scale invariance. Nevertheless, if ω changes as $1/(\sqrt{\lambda}t)$, the time-dependent Schrödinger equation exhibits a space-time scaling symmetry under the transformation $r \to \Lambda r$ and $t \to \Lambda^2 t$.

Defining the cloud size as $\hat{R}^2 = \sum_i \mathbf{r}_i^2/N$, the equation-of-motion for $\hat{R}^2$ can be derived as $i\frac{d}{dt}\langle\hat{R}^2\rangle = \langle[\hat{R}^2, \hat{H}(t)]\rangle = \frac{2i}{N}\langle\hat{D}\rangle$, where $\hat{D} = \sum_i \frac{1}{2}(\mathbf{r_i}\cdot\mathbf{p_i} + \mathbf{p_i}\cdot\mathbf{r_i})$ is the generator of a spatial scaling transformation. Using the fact that the system is scale invariant, and by taking higher-order time derivatives of $\langle\hat{R}^2\rangle$, we conclude that the cloud size $\langle\hat{R}^2\rangle$ obeys the differential equation (see supplementary text S1):

$$\frac{d^3}{dt^3}\langle\hat{R}^2\rangle + \frac{4}{\lambda t^2}\frac{d}{dt}\langle\hat{R}^2\rangle - \frac{4}{\lambda t^3}\langle\hat{R}^2\rangle = 0 \qquad (1)$$

In the experiment, we start with a finite initial trap frequency ω_0 before turning it down (Fig. 1B). The system is at equilibrium for $t < t_0$, and at $t = t_0^+$, $\langle\hat{R}^2\rangle(t_0) = R_0^2$ and $\frac{d^m}{dt^m}\langle\hat{R}^2\rangle|_{t=t_0} = 0$ for $m = 1, 2$. This sets a boundary condition for Eq. 1 that can turn its continuous scaling symmetry in the time domain into a discrete one.

The solution of Eq. 1 can be generally written in a form as $\langle R^2(t)\rangle = C_1 f_1^2 + C_2 f_1 f_2 + C_3 f_2^2$ (The constants C_1, C_2, and C_3 are determined by the boundary conditions), where f_1 and f_2 are two linear independent solutions (see supplementary text S1) of

$$\frac{d^2 f}{dt^2} + \frac{1}{\lambda t^2} f = 0 \qquad (2)$$

By replacing $f(t)$ with $\psi(r)$ and t with r and regarding ψ as a real wave function and r as the hyper-radius, Eq. 2 becomes the zero-energy

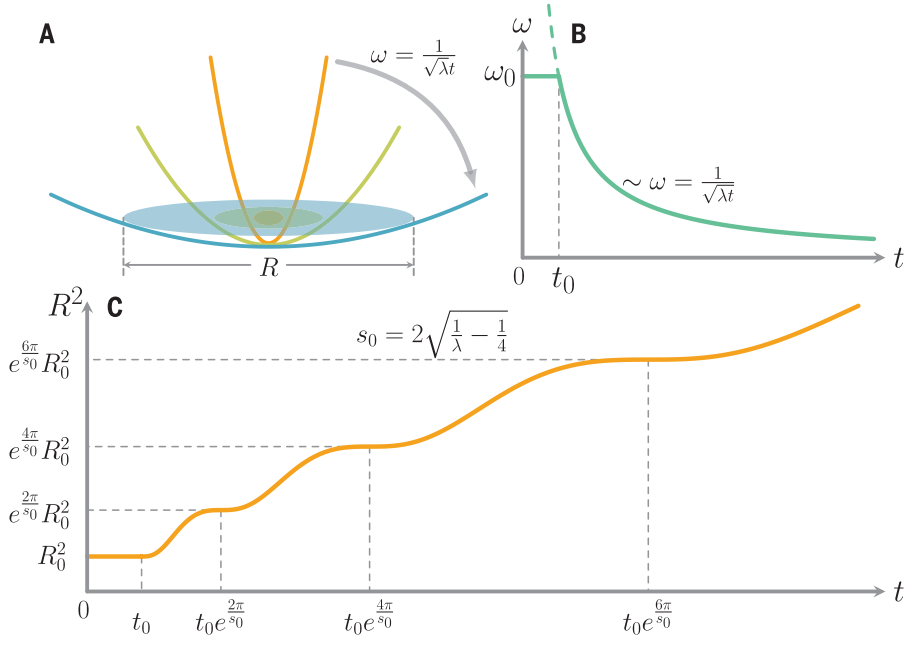

Fig. 1. The schematic of the Efimovian expansion. (**A** and **B**) A scale-invariant ultracold gas is first held in a harmonic trap with frequency ω_0. Then, starting from $t_0 = 1/(\sqrt{\lambda}\omega_0)$, the trap frequency starts to decrease as $1/(\sqrt{\lambda}t)$, and the cloud expands. (**C**) The theoretical predication of the Efimovian expansion: The cloud size $\mathcal{R}$ as a function of time t follows a log-periodic function and exhibits a series of plateaus. The locations of the plateaus obey a geometric scaling law.

[1]State Key Laboratory of Precision Spectroscopy, East China Normal University, Shanghai 200062, P. R. China. [2]Institute for Advanced Study, Tsinghua University, Beijing 100084, P. R. China. [3]Department of Physics, Renmin University of China, Beijing 100872, P. R. China. [4]Collaborative Innovation Center of Extreme Optics, Shanxi University, Taiyuan 030006, China.
*These authors contributed equally to this work. †Corresponding author. Email: qiran@ruc.edu.cn (R.Q.); hbwu@phy.ecnu.edu.cn (H.W.)

Schrödinger equation for the Efimov effect in the hyperspherical coordinate (*14*, *15*). This reveals a connection between this dynamical expansion and the Efimov problem. $\lambda = 4$ is a special point for Eq. 2. For $\lambda < 4$, there are two independent solutions of Eq. 2, $f_1 = \sqrt{t}\cos((s_0/2)\ln t)$ and $f_2 = \sqrt{t}\sin((s_0/2)\ln t)$, where $s_0 = 2\sqrt{1/\lambda - 1/4}$; $\langle R^2 \rangle$ then takes a log-periodic form

$$\frac{\langle \hat{R}^2 \rangle(t)}{R_0^2} = \frac{t}{t_0}\frac{1}{\sin^2\varphi}[1 - \cos\varphi \cdot \cos(s_0 \ln\frac{t}{t_0} + \varphi)] \quad (3)$$

where $\varphi = -\arctan s_0$ is determined by the boundary condition at $t = t_0$. Equation 3 clearly reveals the discrete scaling symmetry—i.e., when $t_2 = e^{2\pi/s_0} t_1$, $\langle \hat{R}^2 \rangle(t_2) = e^{2\pi/s_0} \langle \hat{R}^2 \rangle(t_1)$, and $\frac{d^m}{dt^m}\langle \hat{R}^2 \rangle|_{t=t_2} = e^{-2\pi(m-1)/s_0} \frac{d^m}{dt^m}\langle \hat{R}^2 \rangle|_{t=t_1}$ for all the m-th order derivatives. Therefore, at time $t_n = e^{2\pi n/s_0} t_0$, the first- and second-order time derivatives for $\langle \hat{R}^2 \rangle$ become zero and the cloud expansion is strongly suppressed, that is to say, the expansion dynamics shows a series of plateaus around each t_n. A similar conclusion can also be obtained from the hydrodynamics expansion equations (*34*, *35*). Note that s_0 is tunable by the speed of the decrease of the trap frequency $\omega(t)$. When $\lambda > 4$, $\langle \hat{R}^2 \rangle$ simply follows a power law as $\langle \hat{R}^2 \rangle(t) \sim t^{1+\eta}$ for $t \gg t_0$, where $\eta = \sqrt{1 - 4/\lambda}$. A detailed comparison between this expansion and the Efimov effect is summarized in table S1. We will refer to this effect as the Efimovian expansion.

In our experiment, we use a balanced mixture of ^{6}Li fermions in the lowest two hyperfine states $|\uparrow\rangle \equiv |F = 1/2, M_F = -1/2\rangle$ and $|\downarrow\rangle \equiv |F = 1/2, M_F = 1/2\rangle$. Fermionic atoms are loaded into a cross-dipole trap to perform evaporative cooling. The resulting potential has a cylindrical symmetry around the z axis, and the trap anisotropic frequency ratio ω_r/ω_z is about 9. The above theoretical considerations hold for the isotropic case, but similar results can be obtained for an anisotropic trap (see supplementary text S2). Starting at the initial time t_0, the trap potential is lowered as

$$V(r) = \frac{m}{2\lambda_r t^2} r^2 + \frac{m}{2\lambda_z t^2} z^2 \quad (4)$$

Because $\lambda_r/\lambda_z = (\omega_z/\omega_r)^2 \ll 1$ the effect is more pronounced along the axial direction than in the transverse direction. Therefore, hereafter we focus on the cloud expansion along the axial direction. Theory shows (see supplementary text S2) that the axial cloud square size $\mathcal{R}_z^2$ obeys the same form as Eq. 3, except

$$s_0 = \omega_b \sqrt{1/\lambda_z - 1/4} \quad (5)$$

where ω_b is a factor related to the breathing mode frequency, $\omega_b = 2$ for the noninteracting gas, and $\omega_b = \sqrt{12/5}$ for the unitary Fermi gas along the axial direction. A Feshbach resonance is used to tune the interaction of the atoms either to the noninteracting regime with the magnetic field B = 528 G or to the unitary regime with B = 832 G. The trap frequency is lowered by decreasing the laser intensity, and λ_z is controlled by the decrease rate of the laser intensity, with the initial axial trap depth always fixed at 5% U_0, where U_0 is the full trap potential. Thus, different λ_z corresponds to different $t_0 = 1/(\sqrt{\lambda_z}\omega_z^0)$, where ω_z^0 is the initial axial trap frequency. Finally, after certain expansion time t_{exp} with the trap, the trap is completely turned off and the cloud is probed by standard resonant absorption imaging techniques after a time-of-flight expansion time t_{tof} = 200 μs. Each data point is an average of five shots of the measurements at identical parameters.

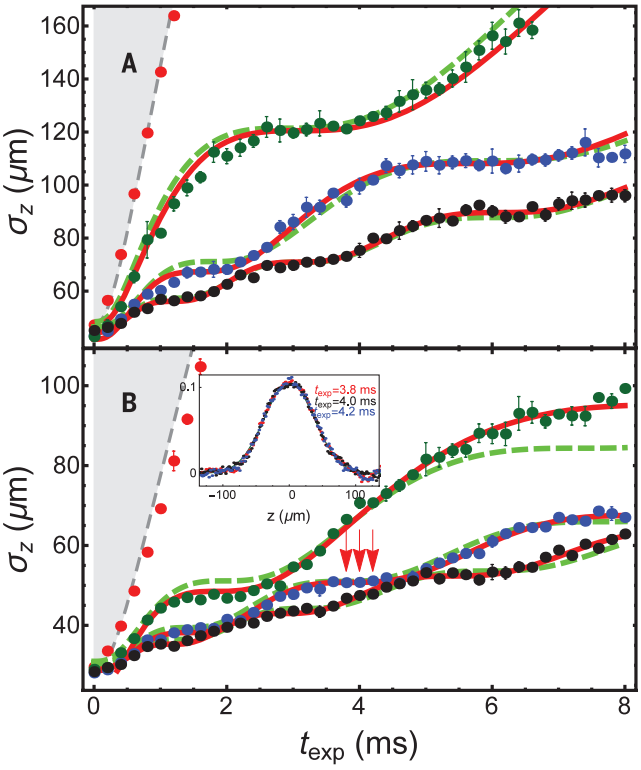

Fig. 2. Experimental observation of the Efimovian expansion. The mean axial cloud size σ_z (with $\sigma_z^2 = 2\langle \hat{R}_z^2 \rangle$) versus the expansion time $t_{exp} = t - t_0$ for (**A**) a noninteracting Fermi gas of ^{6}Li measured at B = 528 G and (**B**) a unitary Fermi gas measured at B = 832 G. Dots are measured data. Black, blue, and green dots denote λ_z = 0.02, 0.07, and 0.36 for (A), and λ_z = 0.01, 0.02, and 0.06 for (B). The dashed lines are the theory curves based on Eq. 3 (with s_0 given by Eq. 5) without any free parameters, and the solid lines are the best fit using the function form of Eq. 3, with s_0 as a fitting parameter. Red dots in both figures denote the case with $\lambda_z = 4$, and the shaded area is the regime where expansion does not show discrete scaling symmetry. The inset in (B) shows three successive density profiles (after the time-of-flight) when the time t_{exp} is located inside a plateau, as indicated by the arrows. Error bars, mean ± SD.

The time-of-flight density profile along the axial direction is fitted by a Gaussian function as $A_0 + A_1 e^{-z^2/\sigma_z^2}$, from which we obtain $\sigma_{z,obs}$. $\sigma_{z,obs}$ is related to the in situ cloud size by a scale factor b_z via $\sigma_{z,obs} = b_z(t_{tof})\sigma_z$; $b_z(t_{tof})$ can be obtained from either hydrodynamic or ballistic expansion equation with the time-of-flight time t_{tof} (see supplementary text S5). Because the trap is quite anisotropic, the cloud expands slowly along the axial direction during a short time-of-flight, and the expansion factor b_z only gives a quantitative correction to the results. Figure 2 shows the typical measurements of σ_z with different λ_z for both the noninteracting and the unitary Fermi gases. For instance, for $\lambda_z = 0.06$, we decrease the trap frequency from $2\pi \times 567.3$ Hz to $2\pi \times 71.0$ Hz within 8 ms. Dots are the measured data, and the solid and the dashed lines are both theoretical curves based on Eq. 3, taking s_0 as a fitting parameter or using s_0 given by Eq. 5, respectively. Because σ_z is obtained by a Gaussian fit to the density profile, $\sigma_z^2 = 2\langle \hat{R}_z^2 \rangle$, and thus the theoretical expression for $\sigma_z/\sigma_{z,0}$ is simply a square root of Eq. 3. Figure 2 clearly shows the plateaus for the expansion dynamics and an excellent agreement between theory and experiment. Density profiles for three successive measurement times inside a plateau almost perfectly overlap with each other (Fig. 2B, inset), which confirms that the expansion stops at the plateau.

For smaller λ_z, the trap frequency decreases slower, the plateaus become denser, and the difference in height between two adjacent plateaus becomes smaller. The adiabatic limit is reached for $\lambda_z \to 0$, where the mean square of the cloud size follows a linear expansion as expected.

For the critical value $\lambda_z = 4$ (red dots in Fig. 2), no plateaus are observed within finite expansion time. How the plateaus disappears as $\lambda_z \to 4$ could not be measured here. This is because as $\lambda_z \to 4$, s_0 decreases toward zero, the period increases exponentially, and therefore even the first plateau would appear after a very long expansion time. On the other hand, there is a lower limit for the trap frequency below which atoms cannot be trapped. Together with the fact that the larger the λ_z, the faster the trapping frequency drops and the shorter the expansion time, the plateaus could not be observed even before reaching the critical value $\lambda_z = 4$ within the finite expansion time. Nevertheless, for comparison, we have performed measurements where the trapping frequency decreases with similar average speeds in Fig. 2, but the time dependence of $\omega(t)$ is different from $1/t$, which breaks the aforementioned

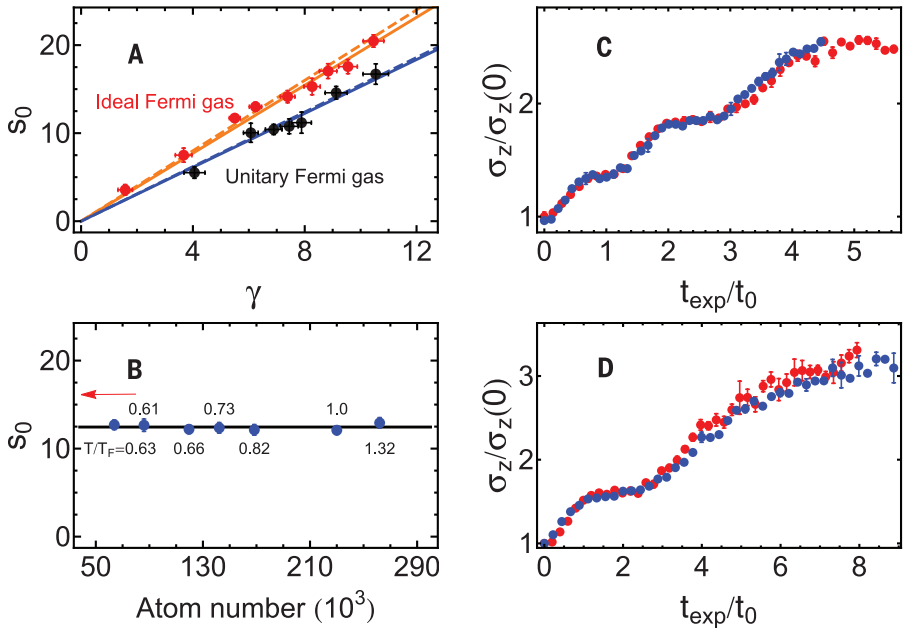

Fig. 3. Universality of the Efimovian expansion. (**A**) s_0 obtained from fitting the expansion curves v.s. $\gamma \equiv \sqrt{1/\lambda_z - 1/4}$. The solid lines are the linear fitting curves, and the dashed lines are $s_0 = \omega_b\gamma$, with $\omega_b = 2$ for the noninteracting fermions and $\omega_b = \sqrt{12/5}$ for the unitary Fermi gas. (**B**) For a given $\lambda_z = 0.017$ and for the unitary Fermi gas, s_0 is obtained from fitting the expansion curves for different fermion numbers and temperatures as indicated (T_F is the Fermi temperature). The solid line is the theory value for the unitary Fermi gas, and the arrow indicates the theory value for the noninteracting Fermi gas with the same λ_z. $\sigma_z/\sigma_{z,0}$ as a function of t_{exp}/t_0 for the noninteracting (red dots) and the unitary Fermi gas (blue dots) with $s_0 = 10.53$ in (**C**) and $s_0 = 5.88$ in (**D**). Error bars, mean ± SD.

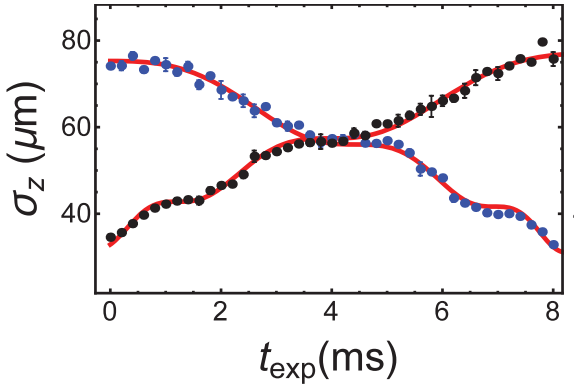

Fig. 4. Time-reversal symmetry of the Efimovian expansion. σ_z for the expansion and its inverted compression process from t_0 to t_f. $t_{exp} = t - t_0$. Black dots are the expansion process, with $\omega = 1/(\sqrt{\lambda}t)$ and the frequency changing from $\omega_0 = 1/(\sqrt{\lambda}t_0)$ (at t_0) to $\omega_f = 1/(\sqrt{\lambda}t_f)$ (at t_f). Blue dots are the inverted compression process, with $\omega = 1/(\sqrt{\lambda}(t_f + t_0 - t))$ and the frequency changing from ω_f (at t_0) to ω_0 (at t_f). Here, $\lambda_z = 0.01$ and the data are taken in the unitary regime. Error bars, mean ± SD.

spatial-time scaling symmetry. The plateaus are indeed not observed in the expansion (fig. S2).

We now demonstrate that these dynamics are universal. First, we should verify that s_0 relates to λ_z via Eq. 5. In the experiment, λ_z is determined by the trap frequencies measured by the parametric resonance, and s_0 is extracted from the best fit of the expansion data in Fig. 2. The universal relation between s_0 and $\gamma \equiv \sqrt{1/\lambda_z - 1/4}$ is plotted in Fig. 3A. $s_0(\gamma)$ can fit very well with a linear function $s_0 = \kappa\gamma$, which gives the slope $\kappa = 1.94 \pm 0.03$ for the noninteracting case and $\kappa = 1.53 \pm 0.03$ for the unitary Fermi gas. These are in good agreement with $\omega_b = 2$ for the noninteracting case and $\omega_b = \sqrt{12/5} = 1.55$ for the unitary case. The Efimovian expansion is also robust and insensitive to the temperature and atom number of the Fermi gas (Fig. 3B).

Second, we notice that the noninteracting and the unitary cases only differ in the relation between s_0 and λ, and once s_0 is given to be the same, the dynamics are exactly identical for these two different systems (Fig. 3, C and D). In other words, $\mathcal{R}_z/\mathcal{R}_z(0)$ is a function of s_0 (or φ) and t/t_0 is a universal function for all scale-invariant systems.

Finally, we study a time-reversed compression process. Consider an expansion process from t_0 to t_f, where the trap frequency decreases from $\omega_0 = 1/(\sqrt{\lambda}t_0)$ to $\omega_f = 1/(\sqrt{\lambda}t_f)$. Now we consider an inverted process of increasing the trap frequency as $\omega = 1/(\sqrt{\lambda}(t_f + t_0 - t))$, where the trap frequency increases from ω_f to ω_0 when t changes from t_0 to t_f. For the compression dynamics to really invert the expansion dynamics, t_f has to be carefully chosen to satisfy $t_f = e^{2\pi n/s_0}t_0$. We perform such an experiment (Fig. 4) showing that the dynamical process with a carefully chosen boundary is time-reversal symmetric. The small asymmetry arises because the lowering of the trap during expansion (black dots) causes evaporative cooling, which decreases cloud sizes correspondingly.

Our results are universal for all scale-invariant quantum gases. Future experiments can test them with a Tonks gas in 1D and in a 2D quantum gas, where the deviation from the log-periodic behavior can be used to calibrate the scaling symmetry anomaly in 2D (*36*–*39*). In the 3D case, it will be interesting to investigate the scaling symmetry breaking when the system is tuned away from the scale-invariant points of zero and infinite s-wave scattering length. The study could also be generalized to observe a dynamic analogy of a recently proposed super-Efimov effect (*40*–*42*).

REFERENCES AND NOTES

1. J. Kinast *et al.*, *Science* **307**, 1296–1299 (2005).
2. S. Nascimbène, N. Navon, K. J. Jiang, F. Chevy, C. Salomon, *Nature* **463**, 1057–1060 (2010).
3. M. Horikoshi, S. Nakajima, M. Ueda, T. Mukaiyama, *Science* **327**, 442–445 (2010).
4. N. Navon, S. Nascimbène, F. Chevy, C. Salomon, *Science* **328**, 729–732 (2010).
5. M. J. H. Ku, A. T. Sommer, L. W. Cheuk, M. W. Zwierlein, *Science* **335**, 563–567 (2012).
6. L. A. Sidorenkov *et al.*, *Nature* **498**, 78–81 (2013).
7. C. Cao *et al.*, *Science* **331**, 58–61 (2011).
8. A. Sommer, M. Ku, G. Roati, M. W. Zwierlein, *Nature* **472**, 201–204 (2011).
9. D. Stadler, S. Krinner, J. Meineke, J.-P. Brantut, T. Esslinger, *Nature* **491**, 736–739 (2012).
10. J.-P. Brantut *et al.*, *Science* **342**, 713–715 (2013).
11. M. Koschorreck, D. Pertot, E. Vogt, M. Köhl, *Nat. Phys.* **9**, 405–409 (2013).
12. A. B. Bardon *et al.*, *Science* **344**, 722–724 (2014).
13. E. Elliott, J. A. Joseph, J. E. Thomas, *Phys. Rev. Lett.* **112**, 040405 (2014).
14. V. Efimov, *Phys. Lett. B* **33**, 563–564 (1970).
15. E. Braaten, H.-W. Hammer, *Phys. Rep.* **428**, 259–390 (2006).
16. T. Kraemer *et al.*, *Nature* **440**, 315–318 (2006).
17. S. Knoop *et al.*, *Nat. Phys.* **5**, 227–230 (2009).
18. J. R. Williams *et al.*, *Phys. Rev. Lett.* **103**, 130404 (2009).
19. S. E. Pollack, D. Dries, R. G. Hulet, *Science* **326**, 1683–1685 (2009).
20. M. Berninger *et al.*, *Phys. Rev. Lett.* **107**, 120401 (2011).
21. S. Roy *et al.*, *Phys. Rev. Lett.* **111**, 053202 (2013).
22. R. S. Bloom, M.-G. Hu, T. D. Cumby, D. S. Jin, *Phys. Rev. Lett.* **111**, 105301 (2013).
23. M. Kunitski *et al.*, *Science* **348**, 551–555 (2015).
24. M. Zaccanti *et al.*, *Nat. Phys.* **5**, 586–591 (2009).
25. B. Huang, L. A. Sidorenkov, R. Grimm, J. M. Hutson, *Phys. Rev. Lett.* **112**, 190401 (2014).
26. S. K. Tung, K. Jiménez-García, J. Johansen, C. V. Parker, C. Chin, *Phys. Rev. Lett.* **113**, 240402 (2014).
27. R. Pires *et al.*, *Phys. Rev. Lett.* **112**, 250404 (2014).
28. M. H. Anderson, J. R. Ensher, M. R. Matthews, C. E. Wieman, E. A. Cornell, *Science* **269**, 198–201 (1995).
29. K. B. Davis *et al.*, *Phys. Rev. Lett.* **75**, 3969–3973 (1995).

30. K. M. O'Hara, S. L. Hemmer, M. E. Gehm, S. R. Granade, J. E. Thomas, *Science* **298**, 2179–2182 (2002).
31. C. Fort *et al.*, *Phys. Rev. Lett.* **95**, 170410 (2005).
32. L. Sanchez-Palencia *et al.*, *Phys. Rev. Lett.* **98**, 210401 (2007).
33. M. Greiner, O. Mandel, T. Esslinger, T. W. Hänsch, I. Bloch, *Nature* **415**, 39–44 (2002).
34. Y. Castin, *C. R. Phys.* **5**, 407–410 (2004).
35. L. P. Pitaevskii, A. Rosch, *Phys. Rev. A* **55**, R853–R856 (1997).
36. E. Vogt *et al.*, *Phys. Rev. Lett.* **108**, 070404 (2012).
37. J. Hofmann, *Phys. Rev. Lett.* **108**, 185303 (2012).
38. E. Taylor, M. Randeria, *Phys. Rev. Lett.* **109**, 135301 (2012).
39. C. Gao, Z. Yu, *Phys. Rev. A* **86**, 043609 (2012).
40. Y. Nishida, S. Moroz, D. T. Son, *Phys. Rev. Lett.* **110**, 235301 (2013).
41. A. G. Volosniev, D. V. Fedorov, A. S. Jensen, N. T. Zinner, *J. Phys. At. Mol. Opt. Phys.* **47**, 185302 (2014).
42. C. Gao, J. Wang, Z. Yu, *Phys. Rev. A* **92**, 020504 (2015).

ACKNOWLEDGMENTS

We thank P. Zhang for helpful discussions. This research is supported by the National Natural Science Foundation of China (NSFC) (grant nos. 11374101 and 91536112) and the Shu Guang project (14SG22) of Shanghai Municipal Education Commission and Shanghai Education Development Foundation. Z.S. and H.Z. are supported by MOST (grant no. 2016YFA0301604), Tsinghua University Initiative Scientific Research Program and NSFC grant no. 11325418. R.Q. is supported by the Fundamental Research Funds for the Central Universities and the Research Funds of Renmin University of China under grant no. 15XNLF18 and no. 16XNLQ03.

SUPPLEMENTARY MATERIALS

www.sciencemag.org/content/353/6297/371/suppl/DC1
Materials and Methods
Supplementary Text
Figs. S1 to S3
Table S1
References (*43*, *44*)

13 December 2015; accepted 21 June 2016
10.1126/science.aaf0666

PHYSICS

Electron microscopy of electromagnetic waveforms

A. Ryabov[1,2] and P. Baum[1,2]*

Rapidly changing electromagnetic fields are the basis of almost any photonic or electronic device operation. We report how electron microscopy can measure collective carrier motion and fields with subcycle and subwavelength resolution. A collimated beam of femtosecond electron pulses passes through a metamaterial resonator that is previously excited with a single-cycle electromagnetic pulse. If the probing electrons are shorter in duration than half a field cycle, then time-frozen Lorentz forces distort the images quasi-classically and with subcycle time resolution. A pump-probe sequence reveals in a movie the sample's oscillating electromagnetic field vectors with time, phase, amplitude, and polarization information. This waveform electron microscopy can be used to visualize electrodynamic phenomena in devices as small and fast as available.

Electron microscopy works at wavelengths 100,000× smaller than that of light and therefore allows studying matter and materials with subatomic resolution (*1*, *2*). With added temporal resolution, ultrafast reaction paths in physical and chemical transitions can also be recorded (*3*, *4*).

Rather elusive for electron microscopy, however, have been electrodynamic phenomena, although oscillating currents and fields are fundamental to the operation of almost any information processing device or metamaterial. Based on differential phase contrast (*5*, *6*), ptychography (*7*), or laser-electron energy exchange techniques (*8*), electron microscopy studies on electromagnetism could reveal electrostatic field distributions (*9*–*11*), ultrafast carrier diffusions (*12*, *13*), or cycle-averaged nanophotonic dynamics (*14*–*16*), but so far not the fundamental electromagnetic waveforms with their rapidly oscillating field vectors.

We merged the electron microscope's supremacy in matter characterizations with a subcycle and subwavelength access to electromagnetic phenomena (Fig. 1). Femtosecond electron pulses (Fig. 1, blue) at 70 keV central energy are generated by pulsed-laser photoemission (*17*). The electron wavepackets (*18*) are further compressed in time by a terahertz field (Fig. 1, red) in grazing incidence to a foil (*19*). Alternatives here could be beam blanking (*20*), microwave compression (*18*), photon-gating (*21*), or ponderomotive bunching (*22*). A magnetic lens (Fig. 1, gray) widens the beam for passage through the sample with close-to-zero divergence. The proof-of-principle sample is a metal split-ring resonator (Fig. 1, yellow), which is a typical building block for metamaterials (*23*) or surfaces (*24*) with optical effects otherwise not available (*25*, *26*). The resonator with ~250 μm radius is excited with a single-cycle, phase-locked electromagnetic pulse of 0.1 to 0.8 THz bandwidth (*17*). It propagates along the z axis with a linear polarization oriented ~5° off the y axis. The electron pulse duration at the sample is ~15 times shorter than the excitation half-cycle. An objective magnetic lens (Fig. 1, gray) magnifies the shadowed electron beam onto a screen (Fig. 1, green). Some intentional defocus makes the scheme sensitive to local beam deflections (Fig. 1, dotted lines) and allows concluding from the distorted screen images, taken at a sequence of electron/field delay times, to the time-frozen electrodynamics in the sample.

First results are shown in Fig. 2, obtained with the excitation field depicted in Fig. 2A and at a magnification of about 5×. The electron pulses are characterized by streaking (*19*) and have 80-fs duration (Fig. 2B). The resonator, which was laser-machined into 30-μm-thick aluminum foil (Fig. 2C), shows some imperfections, in particular fringy edges and off-center circles. An isosurface of the time-dependent shadow pattern deformations reveals pronounced temporal oscillations (Fig. 2D). The raw images (shown

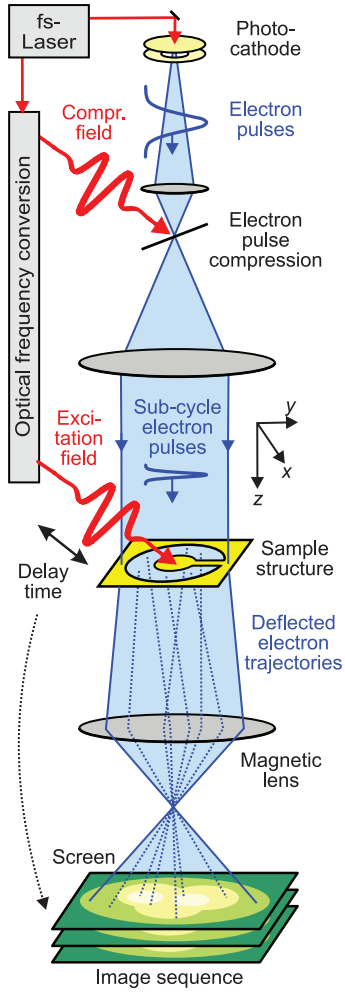

Fig. 1. Concept and experimental setup. A femtosecond laser produces single-cycle terahertz pulses (red) and a beam of femtosecond electron pulses (blue). The terahertz radiation compresses the electrons in time and also triggers electromagnetic resonance in the sample (yellow). The electron pulses are locally and instantaneously distorted (dotted lines) and therefore reveal the electrodynamics of the sample.

[1]Ludwig-Maximilians-Universität München, Am Coulombwall 1, 85748 Garching, Germany. [2]Max Planck Institute of Quantum Optics, Hans-Kopfermann-Straße 1, 85748 Garching, Germany.
*Corresponding author. Email: peter.baum@lmu.de

Science
AAAS

Observation of the Efimovian expansion in scale-invariant Fermi gases

Shujin Deng, Zhe-Yu Shi, Pengpeng Diao, Qianli Yu, Hui Zhai, Ran Qi and Haibin Wu (July 21, 2016)

Science **353** (6297), 371-374. [doi: 10.1126/science.aaf0666]

Editor's Summary

Steps to ultracold gas expansion

Cold atomic gases are often studied while confined in parabolic traps, with the largest atomic density at the center of the trap. When the trap is made shallower, the gas radially expands as the energy cost for atoms that are farther from the trap center decreases. Deng *et al.* observed an interesting effect when they reduced the characteristic frequency of the parabolic trap so that it was at any moment inversely proportional to the elapsed time. Instead of expanding continuously, a strongly interacting Fermi gas held in such a trap stalled at certain time points. These time points formed a geometric progression, a consequence of scale invariance in the strongly interacting limit.

Science, this issue p. 371

Science (print ISSN 0036-8075; online ISSN 1095-9203) is published weekly, except the last week in December, by the American Association for the Advancement of Science, 1200 New York Avenue NW, Washington, DC 20005.